

Research Paper

Vascularized tumor on a microfluidic chip to study mechanisms promoting tumor neovascularization and vascular targeted therapies

Magdalena Skubal¹, Benedict Mc Larney¹, Ngan Bao Phung^{1,3}, Juan Carlos Desmaras¹, Abdul Vehab Dozic¹, Alessia Volpe^{1,2}, Anuja Ogirala¹, Camila Longo Machado^{1,2}, Jakob Djibankov¹, Vladimir Ponomarev^{1,2,3,4}, Jan Grimm^{1,2,3,4}✉

1. Molecular Pharmacology Program, Memorial Sloan Kettering Cancer Center, New York, NY, USA.
2. Department of Radiology, Memorial Sloan Kettering Cancer Center, New York, NY, USA.
3. Department of Pharmacology, Weill Cornell Medical College, New York, NY, USA.
4. Department of Radiology, Weill Cornell Medical College, New York, NY, USA.

✉ Corresponding author: Jan Grimm; grimmj@mskcc.org.

© The author(s). This is an open access article distributed under the terms of the Creative Commons Attribution License (<https://creativecommons.org/licenses/by/4.0/>). See <https://ivyspring.com/terms> for full terms and conditions.

Received: 2024.02.15; Accepted: 2024.11.05; Published: 2025.01.01

Abstract

The cascade of events leading to tumor formation includes induction of a tumor supporting neovasculature, as a primary hallmark of cancer. Developing vasculature is difficult to evaluate *in vivo* but can be captured using microfluidic chip technology and patient derived cells. Herein, we established an *on chip* approach to investigate the mechanisms promoting tumor vascularization and vascular targeted therapies via co-culture of cancer spheroids and endothelial cells in a three dimensional environment.

Methods: We investigated both, tumor neovascularization and therapy, via co-culture of human derived endothelial cells and adjacently localized metastatic renal cell carcinoma spheroids on a commercially available microfluidic chip system. Metastatic renal cell carcinoma spheroids adjacent to primary vessels model tumor, and induce vessels to sprout neovasculature towards the tumor. We monitored real time changes in vessel formation, probed the interactions of tumor and endothelial cells, and evaluated the role of important effectors in tumor vasculature. In addition to wild type endothelial cells, we evaluated endothelial cells that overexpress Prostate Specific Membrane Antigen (PSMA), that has emerged as a marker of tumor associated neovasculature. We characterized the process of neovascularization on the microfluidic chip stimulated by enhanced culture medium and the investigated metastatic renal cell carcinomas, and assessed endothelial cells responses to vascular targeted therapy with bevacizumab via confocal microscopy imaging. To emphasize the potential clinical relevance of metastatic renal cell carcinomas *on chip*, we compared therapy with bevacizumab *on chip* with an *in vivo* model of the same tumor.

Results: Our model permitted real-time, high-resolution observation and assessment of tumor-induced angiogenesis, where endothelial cells sprouted towards the tumor and mimicked a vascular network. Bevacizumab, an antiangiogenic agent, disrupted interactions between vessels and tumors, destroying the vascular network. The *on chip* approach enabled assessment of endothelial cell biology, vessel's functionality, drug delivery, and molecular expression of PSMA.

Conclusion: Observations in the vascularized tumor *on chip* permitted direct and conclusive quantification of vascular targeted therapies in weeks as opposed to months in a comparable animal model, and bridged the gap between *in vitro* and *in vivo* models.

Keywords: microfluidic chip, neovascularization, targeted therapies, confocal imaging, optoacoustic imaging

Introduction

Tumor neovascularization is one of the hallmarks of cancer [1] and constitutes an important

area of cancer research, that aims to understand how cancer cells foster the formation of new supportive

blood vessels [1, 2]. Understanding the biology of tumor associated vasculature is essential to improve vascular targeted therapies frequently investigated as a strategy for cancer treatment [3].

Cancer research was traditionally conducted using two dimensional (2D) cell cultures complemented by *in vivo* animal studies. *In vitro* cultures are valuable tools, but they often fail to reproduce the complexity of cancer phenotypes *in vivo* [4]. Patient-derived xenografts mimic human cancer and are a frequently used tool to evaluate novel therapies, however, they are laborious, and it is expensive to routinely screen tumors from multiple patients. Studies in animals can hinder repeated and precise evaluation of the complex tumor microenvironment (TME) elements, particularly the tumor vasculature. Consequently, whilst these conventional models enable the evaluation of highly specific questions, their inherent limitations frequently hinder the accurate translation of findings to clinical outcomes [5, 6]. A potential way to approach this challenge is to replicate the functional microenvironment *in vitro* using a combination of human derived cultures and microfluidic chip (MFC) technology [7]. In particular, three dimensional (3D) cultures such as cell spheroids, organoids and tumoroids provide relevant and highly controllable cancer models to expedite drug discovery and evaluation [5, 8-11]. MFC technology may not completely replace established *in vitro* and *in vivo* methods but is a powerful supplement permitting rapid insights. It enables the replication of the physiology and pathophysiology of individual human organs such as blood vessels [12-14], brain [15-17], heart [18], lung [19, 20], intestine [21, 22], liver [23, 24], kidney [18, 25], or multiple organs connected by vascular flow [26]. Furthermore, the nature of the MFC provides an opportunity for precision medicine, such as patient specific assessment of drug response, or personalized strategies for disease prevention [27, 28].

In this work, we have established an approach to investigate both tumor neovascularization and therapy via co-culture of human endothelial cells (EC) together with adjacently localized cancer cell spheroids, on a commercially available MFC system. The small footprint of the MFC technology, up to 12 replicates per incubator, no need for animal protocol approval, quick turnaround, and versatility allows tumor research by labs unable to access animal facilities. The MFC technology enables cutting-edge research without reducing its impact or relevance. Additionally, the commercial aspect of systems like the one used here aids in ensuring replicability and multi-lab use. In this MFC model, there are no

performed vascular structures or guides other than two primary channels that are seeded with EC and perfused continuously with culture medium, comparable to other MFC systems [29, 30]. Cancer cell spheroids adjacent to these primary vessels model an early tumor and induce vessels to sprout towards the tumor. Therefore, all processes are following the cascade of events happening in a living being, but under controlled conditions and constant observation. The platform used in this work supports relevant culture parameters, lumenally perfused microvasculature and the ability to intravascularly deliver compounds. Tumor size, degree of vascularization, and compound delivery can be constantly monitored using confocal microscopy. Establishing a vascularized tumor on the MFC permits modeling of the tumor along with its vasculature, whilst constant medium flow maintains mechanical forces like those experienced by cells *in vivo*. Within systems like ours cells are migrating, coordinating, and organizing themselves into 3D tumor-vascular entities. We can readily create a simple microenvironment, monitor real time changes in vessel formation, probe the interactions of tumor and endothelial cells, and evaluate the role of important effectors in tumor vasculature. For example, Prostate Specific Membrane Antigen (PSMA), that has emerged as a marker of tumor associated neovasculature.

As a cancer model, we chose a highly vascularized renal cell carcinoma (RCC), the 10th and 13th most common cancer in men and women respectively, with a high mortality rate [31]. In the case of metastatic RCC (mRCC), which comprises 30% of all RCC cases, the 5-year survival rate drops below 20% [32]. *In vivo* mRCC experimentation is hindered by slow growing animal models. Due to the prevalence and complexity of preclinical models, there is an unmet need for rapid and high throughput mRCC models for the assessment of treatment efficacy and biological mechanism elucidation.

PSMA is a transmembrane glycoprotein with a glutamate carboxypeptidase (GCPII) and folate hydrolase enzyme activity [33]. Upregulated PSMA expression is a characteristic of prostate cancer and is associated with prostate cancer progression, metastasis, and poor prognosis in patients [34-36]. PSMA is absent on the surface of normal EC, but PSMA expression in tumor neovasculature is a common feature in a variety of solid cancers and their metastatic sites, including brain, breast, lung, pancreas, bladder, or renal carcinomas [37-41]. Additionally, recent studies have shown that PSMA positive vesicles released from cancer cells are able to induce a high-angiogenic state and PSMA expression in EC [42, 43]. Therefore, in addition to wild type EC,

we evaluated EC that overexpress PSMA. We characterized the process of neovascularization on the MFC stimulated by enhanced culture medium, associated with mRCC, and assessed EC response to vascular targeted therapy with bevacizumab via confocal microscopy imaging.

To emphasize the potential clinical relevance of mRCC on the MFC model, we compared therapy with bevacizumab on the MFC with an *in vivo* model of the same tumor. Since bevacizumab is known to directly affect tumor vasculature [44], we assessed the vascular changes *in vivo* via Raster Scanning

Optoacoustic Mesoscopy (RSOM) [45], a high-resolution optoacoustic imaging technology able to image vessels *in vivo*, using hemoglobin as an endogenous contrast agent. The ability to reliably image and quantify vasculature both on the MFC and *in vivo* enabled a direct comparison of the MFC efficacy to establish methods along with its advantages and limitations. As therapy, we chose bevacizumab, a humanized anti-Vascular Endothelial Growth Factor (VEGF) monoclonal antibody that selectively binds circulating human VEGF and thus inhibits its binding to cell surface receptors on blood

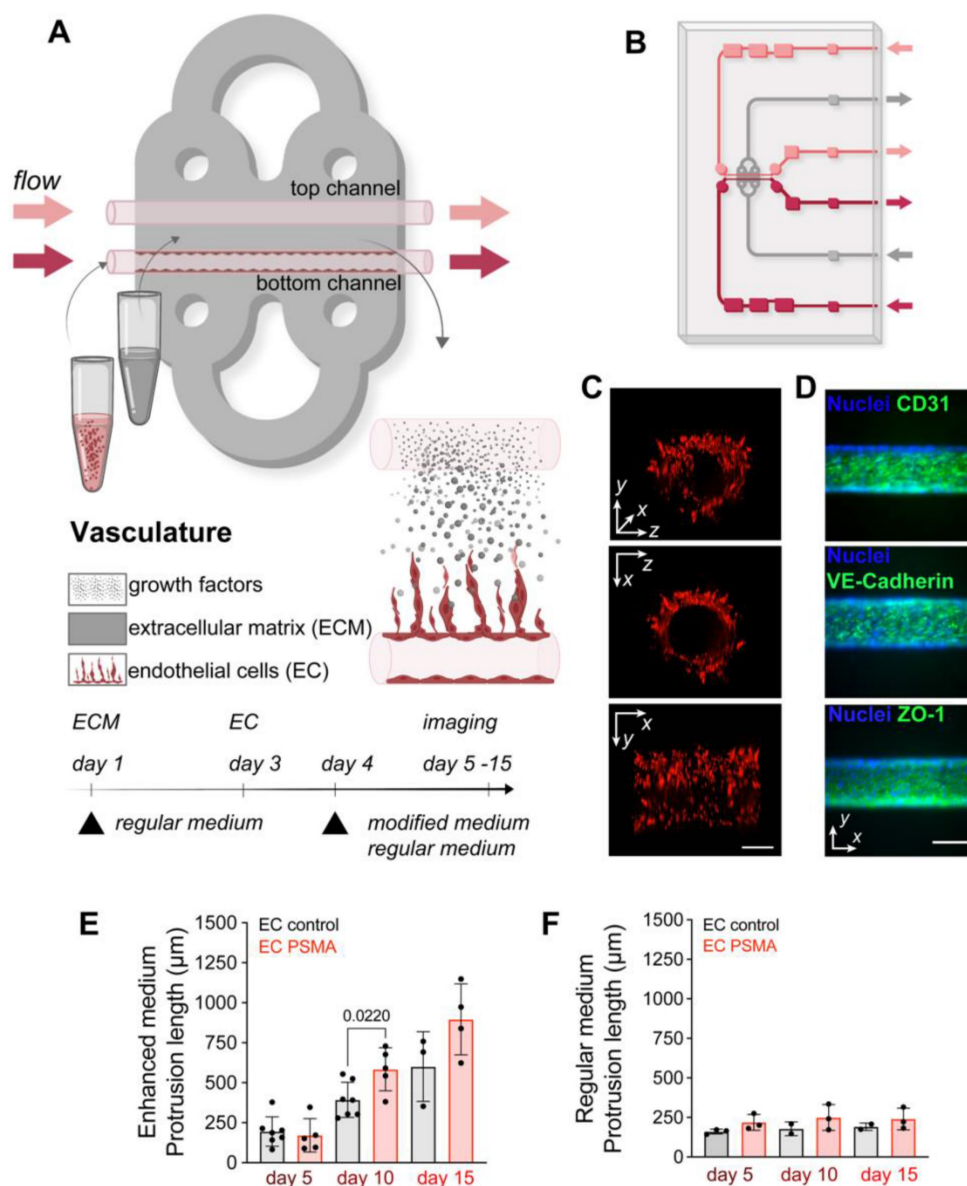


Figure 1: Vascularization model on the microfluidic chip. (A) Visualization and experimental design of vasculature on the MFC. The chip is filled with a collagen-based ECM (gray area) that supports cell growth. Two parallel channels (red and pink, $\phi 100 \mu\text{m}$) at the center of the chip allowed the seeding of EC and mimicked vessels. Arrows indicate the direction of constant flow ($1 \mu\text{L}/\text{min}$). (B) Schematic representation of the double channel MFC system built of ECM (gray area), vessels (red and pink), inlet and outlet ports (red and pink arrows) (detailed description in Figure S1) (C) Representative images of the front, side, and 3D view of the channel with red fluorescent protein (RFP) labeled EC. Scale bar $100 \mu\text{m}$ for all panels. (D) Immunostaining of the organized vessel of endothelial cells EC control confirming the presence of adhesion markers CD31, VE-cadherin and ZO-1 (green) two days after cultured on the MFC system. Scale bars $100 \mu\text{m}$. (E) Quantification of EC control ($n = 7$) and EC PSMA ($n = 5$) showing accelerated cell sprouting when exposed to enhanced medium. (F) Quantification of EC control ($n = 3$) and EC PSMA ($n = 3$) growth when exposed to regular medium. Significance (p) value is based upon a parametric two-tailed unpaired t test.

vessels [44], used in RCC therapy, including first line therapies. A recent study reported that bevacizumab also has the ability to neutralize murine VEGF and to inhibit both angiogenesis and lymphangiogenesis in murine models [46]. VEGF inhibition leads to a reduction in microvascular growth of tumor blood vessels and limits the blood supply to tumor tissues [44]. Using RSOM to image blood vessels, we followed the response of mRCC xenografts from the same mRCC line as used on the MFC, to systemic bevacizumab therapy. RSOM allowed us to characterize the mRCC associated vasculature and monitor the dynamic response to vascular targeted therapy *in vivo*, non-invasively and in real time. We show how the tumor on the MFC allows precise and rapid studies of mechanisms driving tumor neovascularization, permits time and cost-efficient testing of vascular targeted therapies and seamlessly bridges the gap between *in vitro* and *in vivo* models, providing results in a much shorter time frame.

Results

Vascularization on a microfluidic chip

As a first step, we modeled functional vasculature on the MFC. Chips were prepared by filling the chamber with a collagen-based extracellular matrix (ECM) that supports cell growth. Prepositioned glass fibers were removed from the chamber to form two parallel channels ($\phi 100 \mu\text{m}$). The presence of channels allowed for subsequent seeding of cells into the ECM in a replicable and controlled manner, and further permitted to maintain a gradient of nutrients between channels, by perfusing one of the channels with medium containing additional factors. Seeded endothelial cells (EC) attached to the channel walls and formed a tube as the primary vessel, while medium passing through the channels at a constant speed simultaneously mimicked blood flow (Figure 1A-C, Figure S1, S2). Immunofluorescence staining of EC on the MFC system 2 days after seeding also showed expression of EC marker CD31, as well as tight junction markers VE-Cadherin and ZO-1 (Figure 1D). Normal EC do not express PSMA, but its expression was reported in tumor associated neovasculature [37-40]. Here, we considered both, wild type EC lacking PSMA (EC control), and EC engineered to overexpress functional PSMA (EC PSMA) (Figure S3 A-B). To study sprouting of EC on the MFC, EC control or EC PSMA were seeded in the lower channel and were perfused with regular medium, while the opposite channel remained unseeded and void of cells for perfusion with either regular medium or medium supplemented with tumor promoting phorbol 12-myristate 13-acetate

(PMA) and increased concentration of growth factors: Vascular Endothelial Growth Factor (VEGF) and Fibroblast Growth Factor (FGF) (enhanced medium) (Table 1). Perfusion with enhanced medium created a gradient of tumor promoting factors fostering dynamic communication between channels and initiated EC sprouting. As a result, both EC control and EC PSMA were activated to sprout, and the presence of PSMA protein additionally enhanced EC migration (Figure 1, Figure S2). We observed that EC PSMA cells formed vessel-like structures more avidly and sprouted over larger distances in comparison to EC control. The difference between both phenotypes was significant on day 10 and became more prominent on day 15 (Figure 1E). EC control and EC PSMA exposed to only regular medium neither sprouted in the same manner, nor formed vascular networks (Figure 1F, Figure S2). Based on this result, we further concluded that tumor promoting factors in enhanced culture medium were essential to trigger EC sprouting. However, the combination of these factors with PSMA expression distinctly enhanced rapid EC activation and sprouting.

Vascularized tumor on a microfluidic chip

Encouraged by the development of the sprouting vasculature on the MFC, we next established a co-culture of EC with cancer cell spheroids to address the formation of tumor associated vasculature. Expression of PSMA was identified on the surface of blood vessels associated with multiple cancers [37, 39], including highly vascularized renal carcinoma [38, 47]. We chose patient-derived mRCC as a suitable tumor for the co-culture with EC since these tumors are highly vascularized. After confirming the absence of PSMA on the surface of mRCC cells (Figure S3 C-D), we grew the tumor cells under non-adherent conditions to allow the formation of 3D cancer cell spheroids. First, mRCC spheroids mimicking early tumor stages were embedded in the ECM surrounding the chip channels, and the following day EC were seeded in both channels (Figure 2A). To ensure optimal conditions for cell growth, the MFC was initially perfused with mRCC cell medium, and briefly before seeding the EC, the medium was changed to regular EC medium, to promote adherence of the EC and vessel formation. Co-culture of mRCC spheroids and EC on the MFC was maintained for up to 15 days (Figure 2B). For the duration of that time mRCC spheroids were growing (Figure 2C) and EC were sprouting towards the mRCC spheroids forming vessel-like structures (Figure 2D-E, Figure S4). Interestingly, independent of PSMA expression in the presence of the mRCC spheroids, EC control and EC PSMA behaved alike

(Figure 2D-E, Figure S5). Seeing how the MFC system modeled the vascular sprouting, we then evaluated PSMA expression on EC control. PSMA protein was absent on EC control *in vitro* and on the MFC at day 1

(Figure S3 B, Figure S6), but we readily detected PSMA on EC control at day 15 on the surface of the vascular network surrounding the mRCC spheroid (Figure 2F-I).

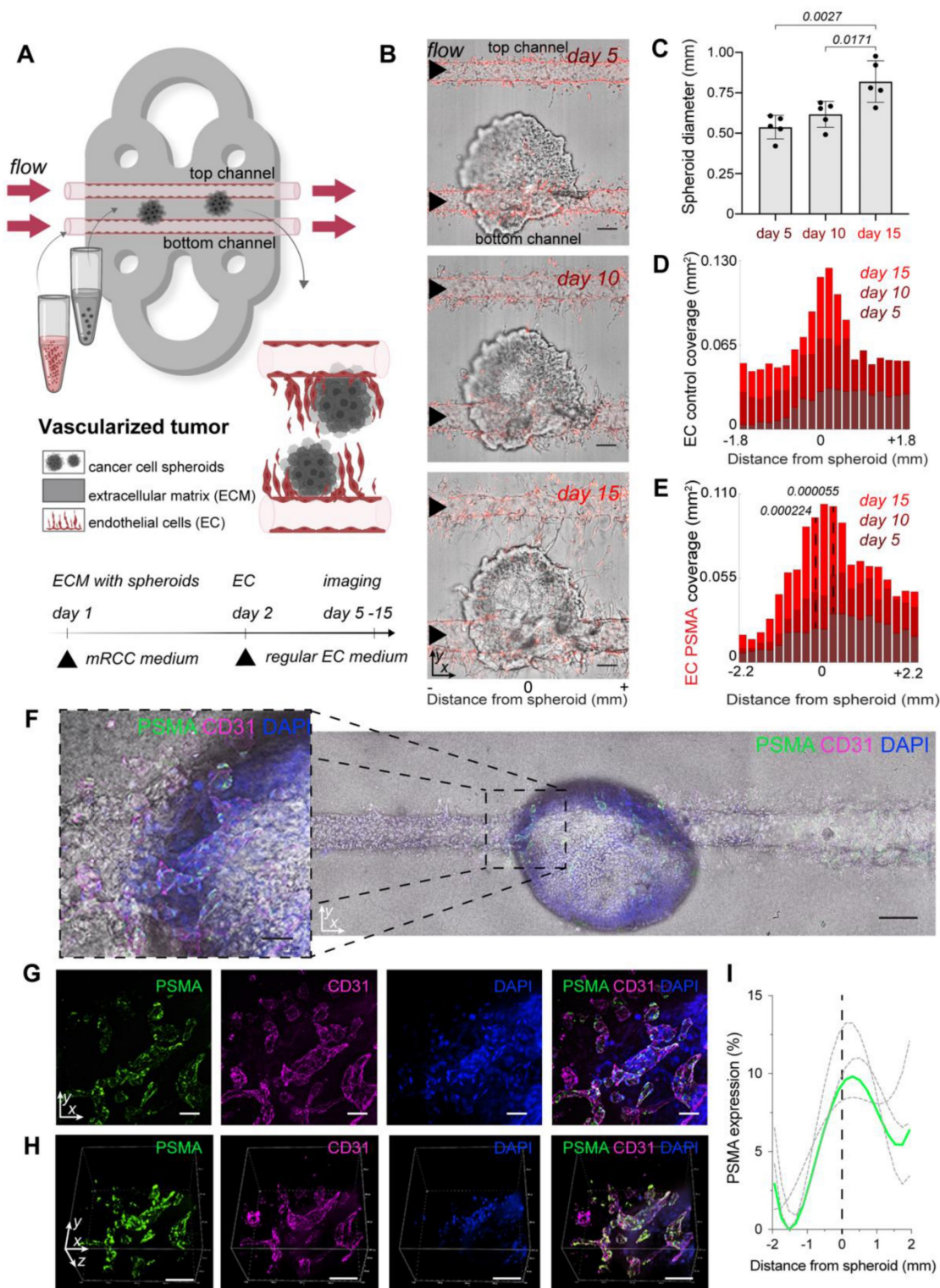


Figure 2: Vascularized tumor model on the microfluidic chip. (A) Schematic visualization of the set-up with vascularized tumor on the MFC. (B) Confocal microscopy images of EC control and mRCC spheroids co-cultured on the MFC at days 5, 10 and 15. (C) Quantification of mRCC spheroid growth (n = 5). (D) Quantification of EC control (n = 3) and (E) EC PSMA (n = 3) sprouting driven by mRCC spheroids. (F) Immunostaining showing PSMA expression on EC control cells co-cultured with mRCC spheroids for 15 days on the MFC. PSMA (green) expression was induced on the newly formed vessels (CD31, magenta) surrounding the mRCC spheroid. Endothelial and cancer cell nuclei stained with DAPI (blue). Scale bars 100 μm. (G) 2D and (H) 3D visualization of PSMA (green), CD31 (magenta) and DAPI (blue) staining. Scale bars 100 μm. (I) Quantification of induced PSMA expression in the area surrounding mRCC spheroid (n = 3). Displayed p values are based upon a two-tailed t test.

Additional immunostainings showed an abundance of PSMA in the proximity and downstream of the mRCC spheroid indicating that factors secreted by the spheroid induced a change in the environment and induction of PSMA expression (Figure S7). As we characterized the model, we also addressed the impact of the flow rate on the formation of vasculature on the MFC. Cells were exposed to a constant flow of 1 $\mu\text{L}/\text{min}$, and we observed a sprouting pattern where EC growth increased with altered distance from the channel entry (highest flow, Figure S8). This pattern is likely in response to altered laminar flow at the inflow and is a characteristic of this system.

Assessment of vessel's functionality and drug delivery on the microfluidic chip

To explore the functionality of tumor associated vasculature, we perfused μm -sized fluorescent beads

through well-developed vasculature on chip and tracked their paths. Beads representing an average size of typical red and white blood cells ($\varnothing 10 \mu\text{m}$ and $\varnothing 15 \mu\text{m}$) were injected through the inlet port and migrated through the vascular network. Beads entered vessels penetrating the surface of the tumor spheroid, demonstrating both the vessel's patency and functionality (Figure 3A-D, Figure S9, S10, Videos 1-3). While the beads modeled blood cells in flowing blood, we next used fluorescein to model the delivery of a small drug molecule to the tumors on the MFC. A tumor on the MFC was first perfused with fluorescein in medium for 120 min for the delivery phase, followed by perfusion with regular EC medium (for 420 min) to wash out fluorescein. Obtained time lapse images demonstrated the clear retention of fluorescence signal in the area occupied by the mRCC spheroid (Figure 3E-G, Video 4-5).

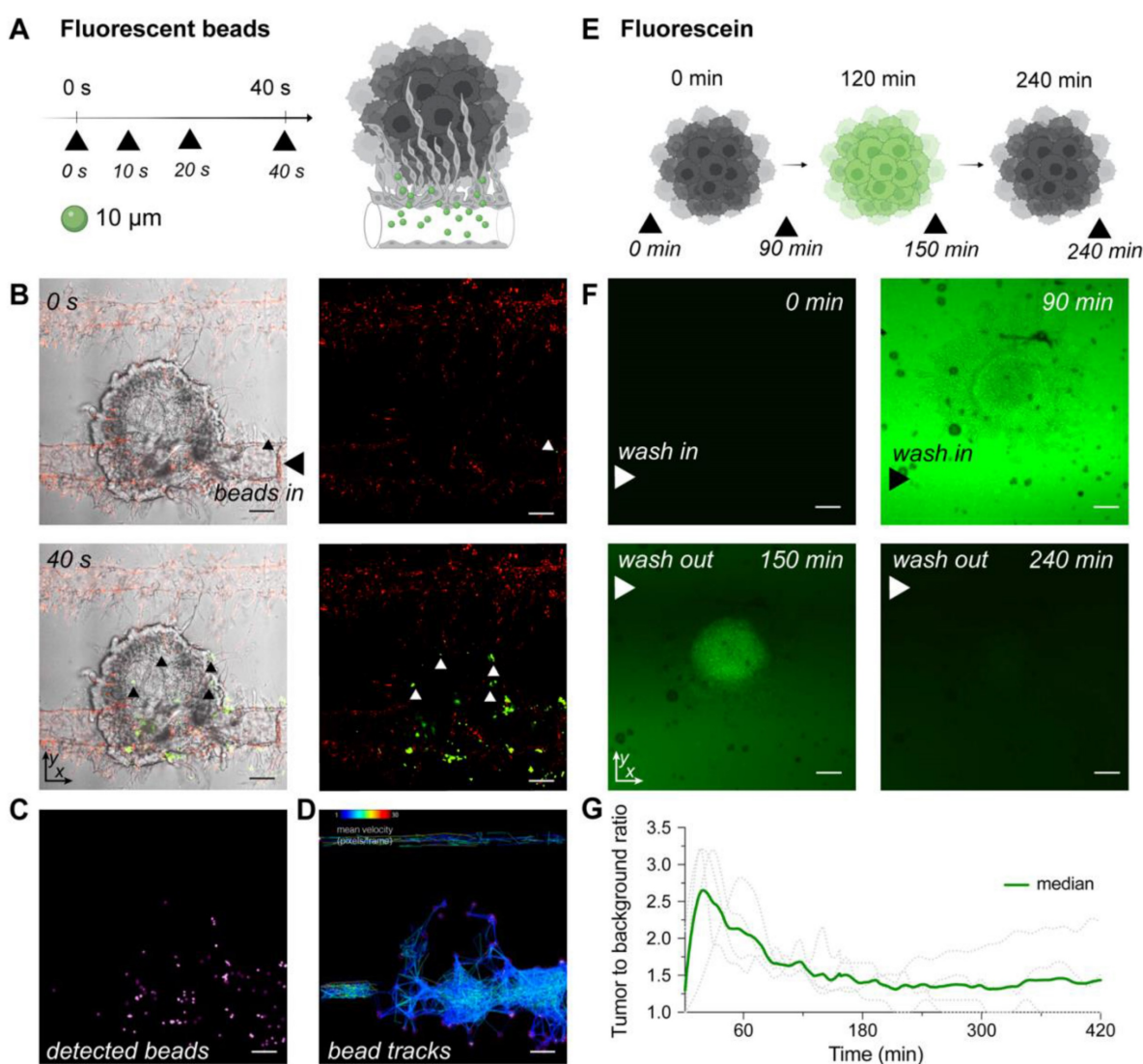


Figure 3: Modelling blood flow and drug delivery. (A) The functionality of tumor associated blood vessels was tested by perfusion of $\varnothing 10 \mu\text{m}$ fluorescent beads representing the size of immune cells. Beads injected into the chip ($n = 1$) with well-developed vasculature (day 15) through the port, entered the chips channels and newly formed

vessels surrounding the surface of tumor spheroid. (B) Confocal microscopy images of beads traveling through the chip captured at 0 s and 40 s after injection (additional timepoints in Figure S9). Left panels represent mRCC spheroids with EC and green fluorescent beads (white light with green fluorescence channel), while the right panels represent red labeled EC with green labeled fluorescent beads (red and green fluorescence channels). Scale bars 100 μm . (C) Beads were tracked while traveling through chip channels and vasculature and became lodged within the vascular network surrounding the cancer spheroid. (D) Beads tracks and their mean speed. (E) Schematic illustration of fluorescence signal retention tested by perfusion of fluorescein (0.001 g/mL) through multiple chips ($n = 4$) at days ranging from 5-10. Fluorescein was pumped into the chip through the bottom channel for 120 min followed by a washing out phase by pumping regular (fluorescein free) medium for 420 min. (F) Confocal microscopy images showing clear fluorescein retention in the mRCC spheroid at 0 min, 90 min (0-120 min fluorescein wash in phase), 150 min and 240 min (120-240 min fluorescein wash out phase). (G) Quantification of fluorescence signal retained in the mRCC spheroids. Scale bars 100 μm .

Simulating vascular-targeted therapy on the microfluidic chip

The vascularized tumor on the MFC model is a promising tool for the assessment of targeted therapy as it opens the possibility to directly target endothelial cells, tumor cells, or mechanisms driving tumorigenesis that cannot be easily explored outside of *in vivo* models. Bevacizumab, a clinically approved therapeutic for advanced RCC is designed to inhibit VEGF and prevents the growth of new blood vessels. Here, mRCC spheroids and EC control cells were co-cultured on the MFC for 9 days followed by perfusion with a regular EC medium or a regular EC medium supplemented with bevacizumab [48]. After 3 days EC in treated chips showed significant destruction, while control chips maintained in regular EC medium (bevacizumab free) throughout the duration of the experiment did not show major changes in the generated vasculature. We were able to image and reconstruct the 3D structure of the vessel highlighting the changes occurring over time (Figure 4).

Vascular targeted therapy *in vivo* as comparison

To assess the translational relevance of the tumor on the MFC approach, we compared it to an *in vivo* mouse model. Using the same mRCC line, we generated xenografts and followed the responses of mRCC tumors to bevacizumab therapy *in vivo*. Tumor volumes were monitored before (100 days) and after treatment (115 days) (Figure 5A). We observed that in comparison to control saline treated mice, tumors in bevacizumab [49] treated mice did not further grow (Figure 5B). Since bevacizumab exerts a direct effect on vasculature by binding VEGF, we employed RSOM, a high-resolution optoacoustic imaging technology, to directly image and quantify blood vessel responses *in vivo*. RSOM enables characterizing tumor vasculature and monitoring the dynamic tumor response to targeted anti-vascular therapy (Figure 5C, Table 2). With RSOM, we were able to assess the effectiveness of the therapy by comparing the vasculature of bevacizumab treated and control tumors, in terms of vessel length, vascular area fraction, branching, tortuosity, and nearest neighbor distance (NND) (Figure 5D-H). We found a significant difference in vascular area fraction between treated

and control tumors (Figure 5E). By comparing the MFC system with the same tumors in an animal model, we confirmed that the MFC modeled the *in vivo* effects well and reduced the assessment of the targeted therapy from nearly 4 months *in vivo* (with this patient-derived xenograft tumor model) to only a few weeks (Figure 4A, Figure 5A). Further *in vivo* comparison of mRCC tumor responses to bevacizumab therapy, showing reduction in vascular coverage is included in Figure S11.

Assessment of angiogenesis-related proteins on the microfluidic chip

The MFC technology provides a highly controlled environment that enables facile assessment of components of the chip perfusate. Here, we employed an angiogenesis-related proteomics analysis to gain further insight into the EC biology, using the following conditions: EC control perfused with regular medium (EC control (Reg)) as a control group, EC control in the presence of the mRCC spheroid perfused with regular medium (EC control + mRCC (Reg)), EC control perfused with enriched medium (EC control (Enriched)), EC PSMA perfused with regular medium (EC PSMA (Reg)) and EC PSMA perfused with enriched medium (EC PSMA (Enriched)) (Table 3, Figure S12). The enriched medium contained increased levels of FGF (basic) and VEGF and accordingly an increasing trend was seen in VEGF and FGF (basic) levels with EC PSMA (Reg) and EC PSMA (Enriched) having the highest expression, however, this was not statistically significant. Also as expected, EC control (Enriched) and EC PSMA (Enriched) had higher expression levels of FGF (acidic), FGF-4 over EC control (Reg) and EC control + mRCC (Reg). Compared to EC control (Reg), EC control (Enriched) additionally showed increased expression of 4 proteins: angiopoietin-1,2, PDGF-AB/PDGF-BB, LAP(TGF- β 1). Meanwhile, EC PSMA (Enriched) displayed higher level of the following 8 proteins: FGF-7, EGF, FGF-basic, endothelin-1, IL-8, LAP (TGF- β 1), MCP-1, and pentraxin 3 (PTX3). Notably, the levels of FGF (basic), EGF, endothelin-1, and IL-8 protein were statistically significantly higher in EC PSMA (Enriched) compared to EC control (Enriched). We also found that EC control + mRCC spheroid (Reg) had 4 proteins statistically significantly overexpressed

compared to all other conditions: DPPIV, IGFBP-3, IL-8, uPA. Furthermore, we also observed that both EC PSMA (Reg) and EC PSMA (Enriched) exhibited lower level of coagulation factor III, CXCL16, and endostatin/collagen XVII compared to both EC control (Reg) and EC control (Enriched). Interestingly,

under the same perfusion conditions, the proteome of EC PSMA (Enriched) revealed statistically significantly lower expression of 5 proteins (angiopoietin-1, CXCL16, endostatin/collagen XVIII, PDGF-AA, and thrombospondin-1) compared to the EC Control (Enriched) (Figure S12, S13).

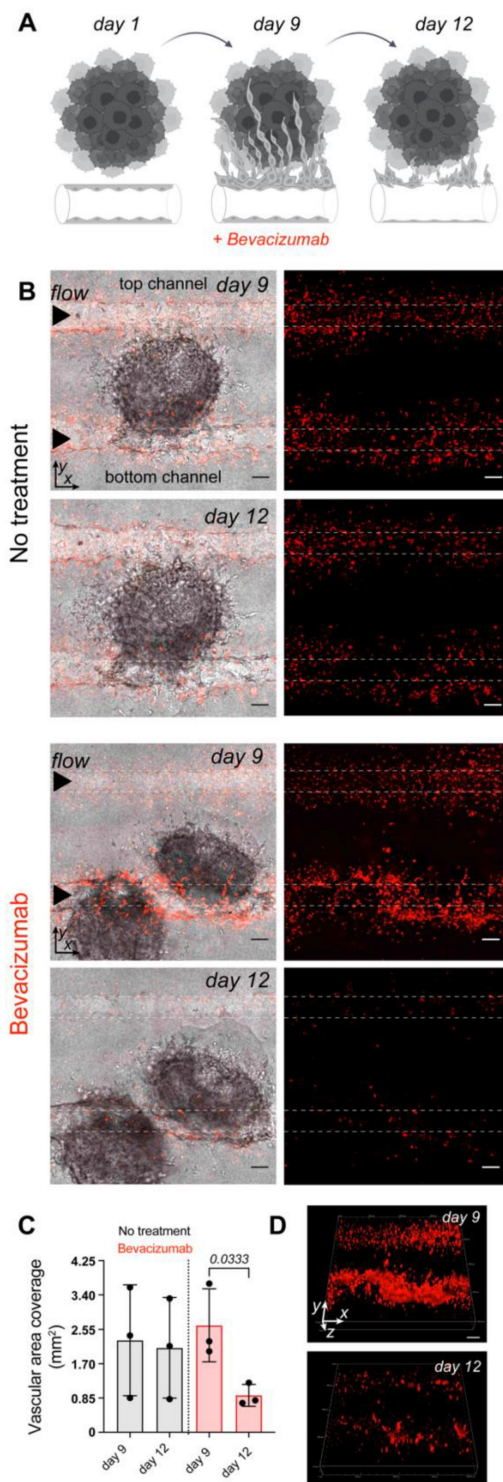


Figure 4: Vascular targeted therapy on the microfluidic chip. (A) The response to vascular targeted therapy on the MFC evaluated by treatment with bevacizumab. EC controls were co-cultured with mRCC spheroids for 9 days followed by perfusion with either regular EC medium (no treatment, $n = 3$) or EC medium supplemented with 250 $\mu\text{g}/\text{mL}$ of bevacizumab (46) ($n = 3$) for 3 days. (B) Confocal microscopy images of chips before (day 9) and after (day 12) bevacizumab treatment. Left panels represent mRCC spheroids (no fluorescence) with endothelial cells (red fluorescence), right panels represent endothelial cells (red fluorescence only). Scale bars 100 μm . (C) Quantification of cell

coverage before and after treatment. (D) 3D visualization of EC response to bevacizumab therapy before (day 9) and after (day 12) treatment. Significance (p) value is based upon a parametric two-tailed t test.

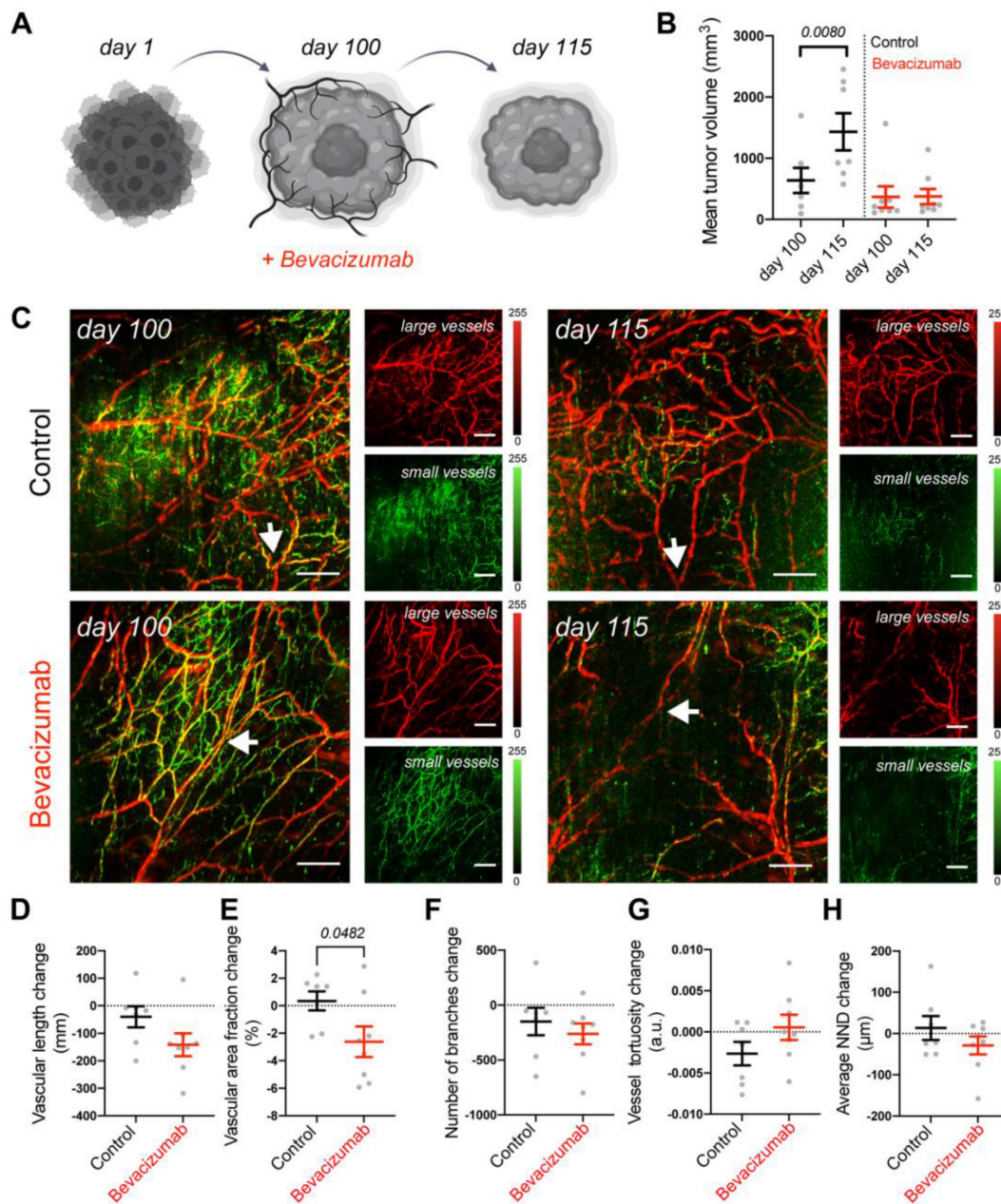


Figure 5: Vascular targeted therapy in vivo. (A) Response of mRCC mouse xenografts to vascular targeted therapy with bevacizumab. (B) mRCC tumors volume measured before and after treatment: mRCC tumors were grown for 100 days before receiving either saline (control group, 50 μ L saline each, $n = 7$) or bevacizumab (treated group, 20 mg/kg bevacizumab [49] in saline each, $n = 8$) 3 times a week for 2 weeks. (C) Representative RSOM images taken 24 h before treatment commencement (day 100), and 24 h after treatment completion (day 115). Images of large vessels (11-33 MHz) and small vessels (33-99 MHz). Scale bars 1 mm. The arrow highlights a tracked vessel for both conditions with the treated mouse showing vessel disruption in response to bevacizumab. Quantification of (D) vascular length, (E) vascular area fraction, (F) number of branches, (G) vessel tortuosity and (H) nearest neighbor distance (NND). Displayed p values are based upon a two-tailed t test.

Table 1: Composition of regular and enriched endothelial cell medium.

Endothelial cell medium	Regular	Enriched
Ascorbic Acid	50 μ g/mL	50 μ g/mL
Hydrocortisone Hemisuccinate	1 μ g/mL	1 μ g/mL
Fetal Bovine Serum (FBS)	2%	2%
L-Glutamine	10 mM	10 mM
Heparin Sulfate	0.75 U/mL	0.75 U/mL
Insulin-like Growth Factor (IGF-1)	15 ng/mL	15 ng/mL
Epidermal Growth Factor (EGF)	5 ng/mL	5 ng/mL

Fibroblast Growth Factor (FGF)	5 ng/mL	30 ng/mL
Vascular Endothelial Growth Factor (VEGF)	5 ng/mL	30 ng/mL
Phorbol 12-myristate 13-acetate (PMA)	-	100 ng/mL

Table 2: Interpretation of RSOM images.

Interpretation of RSOM images	
Red colored vessels	Large and deep vessels, low frequencies
Green colored vessels	Small and shallow vessels, high frequencies
Vascular length	The overall length of the entire vascular networks
Vascular area fraction	The area of the tumor occupied by vessels
Branches	The sprouting nature of the network characteristic of angiogenesis
Vessel tortuosity	Vessel profiling where more tortuous signals a convoluted network
Nearest neighbor distance (NND)	Proximity of vessels to each other

Table 3: Assessment of angiogenesis-related proteins on the microfluidic chip.

Microfluidic chip	Culture conditions, perfused medium	Increased proteins	Decreased proteins
EC control (Reg)	Monoculture of EC control, regular medium	-	-
EC control (Enriched)	Monoculture of EC control, enriched medium	Angiopoietin-1,2, PDGF-AB/PDGF-BB, LAP (TGF- β 1)	-
EC control + mRCC (Reg)	Co-culture of EC and mRCC spheroid, regular medium	DPPIV, IGFBP-3, IL-8, uPA	-
EC PSMA (Reg)	Monoculture of EC PSMA, regular medium	-	Coagulation Factor III, CXCL16, endostatin/collagen XVII
EC PSMA (Enriched)	Monoculture of EC PSMA, enriched medium	FGF-7, EGF, FGF-basic, endothelin-1, IL-8, LAP (TGF- β 1), MCP-1, pentraxin 3 (PTX3)	CXCL16, endostatin/collagen XVII, PDGF-AA, Thrombospondin-1

Discussion

Conventional tumor models often do not accurately reproduce the complexity that affects cancer behavior *in vivo*, and rarely allow for the investigation of individual elements of the TME under controlled conditions, e.g., how cancer cells behave when interacting with EC over time [7]. The MFC technology bridges the gap between *in vitro* and *in vivo* research and creates a space for probing engineered microenvironments of human tissues. Here, we established an approach to model neovascularization and rapidly test vascular targeted therapies on a commercial MFC. To demonstrate the clinical potential, we evaluated the response on the MFC to bevacizumab, a clinically approved therapeutic, and provided its direct comparison to an *in vivo* model. Cytokine-mediated interactions between tumor and EC within the TME define tumor development and progression. The investigation of resistance to anti-vascular biology is essential to improve vascular targeted therapies [50]. Normal EC do not express PSMA, but its overexpression was reported in the neovasculature of numerous cancers [37-40]. This vascular expression of PSMA led us to also consider PSMA expression in our studies. In addition to wild type EC (EC control), we therefore included EC engineered to express PSMA (EC PSMA), mimicking tumor EC in the formation of tumor

neovasculature. We generated a vascularization model on the MFC utilizing human EC, and a vascularized tumor model by adding mRCC spheroids to the system. In the MFC, PSMA positive EC responded more rapidly to environmental stimuli carried in the different culture media, resulting in faster sprouting over larger distances, however by day 15 this difference was less prominent indicating that the biology of PSMA provides an initial growth advantage (where it is most important), which may lead to more rapid vascularization of tumors (Figure 1). Our findings are in line with previous studies reporting that PSMA expression on EC fosters angiogenesis by promoting tube formation, however this has so far only been shown in a 2D culture model [42]. Further, our MFC model showed that a critical component in EC sprouting was enriched medium, supplemented with additional growth factors (VEGF, FGF and PMA), as one example for the kind of molecular investigations that can be achieved with systems like ours.

Growth factors are essential mediators in neovascularization [51-53], and PSMA induces EC sprouting by upregulating matrix metalloproteinases, essential for cell invasion in the early stages of angiogenesis [54]. For the vascularized tumor on the MFC, we combined EC and mRCC spheroids to create a model where endothelial and cancer cells can spontaneously migrate and self-organize to form 3D

structures (Figure 2B). Cancer spheroids more readily allow mimicking aspects of *in vivo* tumor growth that are otherwise not possible to model *in vitro*, particularly neovascularization [55, 56]. To further investigate the effect of PSMA expression on vascularization, we used EC control and EC PSMA, and monitored the real time changes in vessel formation (Figure 2D-E). The comparison between EC control and EC PSMA showed that EC PSMA were growing faster in the direct proximity of the spheroid (Figure S4, S5), in line with the experimentation without spheroids. Otherwise, there was no difference in the response of these EC in the presence of mRCC spheroids with EC controls behaving in a similar manner to EC PSMA. However, the co-culture of EC control and mRCC spheroids induced PSMA expression on EC control (Figure 2F-I, Figure S7). We observed PSMA on the newly formed vessels in the proximity and downstream of the spheroid, as the factors secreted from the mRCC travel downstream of the medium flow direction on the MFC. The exact mechanism by which PSMA gets induced in EC is not yet fully understood. Several studies have found that co-culture of PSMA-negative EC with cancer cells expressing PSMA, such as prostate and breast cancer cells, can transform EC to express PSMA through uptake of PSMA positive membranes, such as microvesicles [42, 43]. Furthermore, co-culture of EC and tumor cells under hypoxic conditions also leads to higher PSMA expression in EC [42, 57]. Although renal cell carcinomas were previously used to study tumor angiogenesis on the MFC [13], we report for the first time that co-culture of EC and mRCC can promote PSMA expression on EC control. Interestingly, as PSMA expression was not observed directly on mRCC cells (Figure S3 C-D), our results suggested that exposure of EC to factors present in culture medium plays an equally important role in microenvironment remodeling in addition to shed vesicles [58]. The functional role of PSMA in angiogenesis remains elusive, but PSMA specific expression on tumor-associated neovasculature suggests that it participates in tumor development and progression [59]. Even while the mechanistic details need to be explored, our data confirms that PSMA provides functional advantages to EC and aids EC sprouting (Figure 1E-F). In summary, we demonstrated the potential of our MFC models to investigate neovascularization and induce neovascular PSMA expression.

Furthermore, collection of perfusate permitted assessment of angiogenesis-related proteins (Figure S12). Importantly, comparing EC control and EC PSMA in the presence of enriched media revealed statistically higher expression levels of 8 proteins

involved in angiogenesis over the other conditions (Figure S13). Remarkably, the expression levels of EGF, endothelin-1 and MCP-1 in EC PSMA enriched medium were more than twice as high compared to other conditions (Figure S13). These findings indicate that PSMA likely enhances the expression of these factors and thus contributes to angiogenesis, as these factors are well-established to enhance endothelial cell proliferation and migration [60-62]. Overall, our studies show that the presence of PSMA on the EC as well as the presence of tumors induced significant changes in the angiogenic protein signatures of the system, shifting it to a more pro-angiogenic state. Interestingly, we saw that endostatin/collagen XVIII decreased when control EC were co-cultured with mRCC in regular medium, and lowest when PSMA was present on the EC in both regular and enriched media (Figure S13). Since endostatin/collagen XVIII is a potent endogenous antiangiogenic factor and can inhibit angiogenesis, this further confirms the observed sprouting results and the induction of a PSMA phenotype in EC control cells in co-culture with mRCC [63]. Overall, models like ours can be helpful in deciphering the role of factors (such as PSMA) involved in angiogenesis.

For personalized medicine applications, reduced throughput in exchange for higher complexity to resemble a tumor with tightly controlled intravascular delivery of candidate therapies is desirable. We first assessed vessel functionality via perfusion with fluorescent beads, representing an average size of typical red and white blood cells (Figure 3A-D) [64]. Beads readily traveled through channels and the vasculature surrounding mRCC spheroids, but mostly failed to penetrate the tumor core as often seen *in vivo* [65]. We provided evidence that the newly formed vessels on the MFC are functional, and study of immunotherapies could be possible with this system. We next addressed the potential of the MFC to model small molecule drug delivery to tumors. To mimic non-targeted therapy, we applied the fluorescent small molecule probe, fluorescein (Figure 3E-G) [66]. Fluorescein is a clinically approved compound utilized in fluorescence guided tumor resection [67]. Fluorescein showed clear tumor delivery, followed by high spheroid retention and finally a wash-out phase in the MFC tumor model, like that seen *in vivo* with e.g., second window ICG imaging [68, 69]. This feature of the MFC setup further emphasizes the recapitulation of *in vivo* environments on the MFC. Attempts to recapitulate this feature without EC were not successful due to non-survival of spheroids in the absence of EC (data not shown).

We proceeded to model vascular targeted therapy. Bevacizumab is used as a first line treatment

in patients with mRCC where it induces a significant improvement in progression free survival [70]. Here, we integrated *in vivo* and *in vitro* imaging methods to evaluate the response of vascularized tumors to bevacizumab, a VEGF inhibitor. Bevacizumab treatment on the MFC successfully blocked EC activation and recruitment, leaving the EC network substantially destroyed within 3 days (Figure 4). Further *in vivo* comparison of the mRCC tumor response to bevacizumab therapy demonstrated clear differences between treated and control tumors (Figure 5A-B). RSOM enabled monitoring of *in vivo* changes in mRCC tumors vasculature (Figure 5C-H). After 2 weeks of treatment, we found a statistically significant difference in vascular area fraction between treated and control tumors. In addition, vascular staining showed similar responses to bevacizumab therapy in mRCC tumors (Figure S11). Bevacizumab affected vessels in a comparable manner on the MFC and *in vivo* but the MFC system allowed us to grow vascularized tumors over 8 times faster than xenografts, and with higher precision to focus on mechanisms driving tumor vascularization. Thus, especially in cases of slow growing cancer xenografts like mRCC, the chip model provides a clear temporal advantage with respect to personalized medicine approaches. For faster growing tumor models this advantage will likely be less pronounced. The MFC approach provides a rapid and reproducible method to grow human relevant models and to screen for suitable treatments, reducing experiment times from nearly 4 months to 2 weeks when compared to mouse models, a valuable time gain for RCC patients.

Results from the MFC and *in vivo* studies allowed for the performance assessment of our system and highlighted its potential for accelerated drug screening and preclinical investigation of biomarker targeting probes. Importantly, the distribution and effects of agents of various sizes (150 kDa to 15 μ m) could be assessed with this MFC. Future iterations of the vascularized tumor on the MFC could facilitate investigations on tumor biology, identify ineffective therapies prior to expensive clinical trial stages, reduce the time needed for the assessment of patient xenograft models and enable a focus on patient tailored, precision cancer medicine. In addition, patient derived organoids on the MFC, used as miniaturized tumor models and avatars for the patient's actual tumor, would allow recapitulation of various aspects of patient physiology and disease phenotypes. These could even be combined with an autologous buffy coat to add immune cells to test immunotherapies thus providing a wide opportunity for improving preclinical drug discovery, and clinical trial validation [71, 72]. Therefore, this work can have

a direct impact on medical research, where it could reduce the requirement for mouse experiments and accelerate translation to clinical research if regulatory institutions accept the impact of MFC systems. We estimate that a single dedicated incubator system could assess around 92 chips in the time required to carry out the *in vivo* experimentation in a footprint like that of two mouse cages (10 mice) increasing throughput by almost an order of magnitude. These aspects of the MFC system are particularly timely considering recent announcements by the FDA (FDA modernization act 2.0) removing the need for animal data prior to commencing clinical trials [73].

However, this MFC system as all preclinical models certainly has limitations. Firstly, setup does require custom installation including pumps, racks, and establishment of the MFC model itself. Secondly, the system does not contain vascular niches to model a more complex tumor microenvironment, a set-up of which is possible but would require modification outside the scope of this work. As a result, the location of spheroids within the chips was random and cannot be controlled. However, spheroids (of similar size due to cell numbers) were added prior to EC seeding and based on our analysis do actively recruit ECs. Thirdly, we co-cultured only cancer and endothelial cells limiting the assessment of immune cells on this work. Additional or alternative components can be added, such as components of the immune system. Local stromal cells and pericytes were previously incorporated on this MFC [74]. A wealth of insights and research has been possible thanks to patient-derived xenografts in immunodeficient mice and MFC may readily provide further discoveries [75]. In cases where *in vivo* insights are still required, preliminary MFC results with this or other systems can be used to guide and optimize this research reducing overall animal numbers used. In drug discovery pipelines the MFC could provide a reliable method for patient derived tumor growth with numerous treatments being investigated in a rapid and high throughput set-up, resulting in accelerated personalized medicine approaches for individual patients.

Materials and Methods

Cell culture

Primary human umbilical vein endothelial cells (EC) were purchased from Angio-proteome (#cAP-0001RFP). Endothelial cells (EC control) were engineered by retroviral gene transfer to stably overexpress functional PSMA protein (EC PSMA) (Figure S3). Cell culture was maintained in a humidified incubator at 37 °C, 5% CO₂ in the EC

medium: VasuLife Basal Medium (Lifeline Cell Technology #LM-0002) supplemented with VEGF kit (Lifeline Cell Technology #LS-1020) containing Ascorbic Acid (50 $\mu\text{g}/\text{mL}$), Hydrocortisone Hemisuccinate (1 $\mu\text{g}/\text{mL}$), Fetal Bovine Serum (FBS; 2%), L-Glutamine (10 mM), Heparin Sulfate (0.75 U/mL) and human recombinant Fibroblast Growth Factor (FGF; 5 ng/mL), human recombinant Insulin-like Growth Factor (IGF-1; 15 ng/mL), human recombinant Epidermal Growth Factor (EGF; 5 ng/mL), human recombinant Vascular Endothelial Growth Factor (VEGF; 5 ng/mL). Enhanced medium was supplemented with additional VEGF (25 ng/mL), FGF (25 ng/mL) and phorbol 12-myristate 13-acetate (PMA, 100 ng/mL) (Table 1). For all performed experiments EC did not exceed 3 passages.

Patient-derived metastatic renal cell carcinoma (non-pooled) JHRCC62A (mRCC) [76] was kindly provided by the Abraham Hakimi Lab (MSKCC). mRCC culture was maintained in a humidified incubator at 37 °C, 5% CO₂ and was supplemented with complete DMEM/F12 medium (Corning #10-103) containing 10% Fetal Bovine Serum (GeminiBio #100-106), 1% L-Glutamine (Gibco #25030081) and 1% Penicillin/Streptomycin (Corning #30-002).

Microfluidic system to create vascularization and vascularized tumor model

The MFC system by Nortis Inc. (Woodinville, WA) was used to establish vasculature and the vascularized tumor models. Our studies are in line with previous work with EC on this platform [74, 77]. To model vasculature on the MFC, extracellular matrix (ECM), the foundation for the sprouting cells, was prepared by mixing chilled collagen I (Corning #354249) with phosphate buffered saline (PBS, Corning #46013CM), phenol red solution (Cepharm Life Sciences #10387-0) and water to the final concentration of 7 mg/mL. Collagen was chosen on account of its mechanical stability and for its fibrillar nature. Additionally, it is less susceptible to the known inconsistencies of Matrigel and was well established for similar applications [13, 78, 79]. Collagen density, thus pH of ECM solution was carefully adjusted to 8-8.5 by adding 1M NaOH. Prior to injection of ECM to the chip, the matrix chamber was washed with 100% ethanol and dried. Approximately 250 μL of ECM solution was injected using chilled 1 mL syringe with 20-gauge blunt needle (McMaster-Carr # 75165A677). The ECM chamber was sealed, and the chip was incubated overnight at room temperature to allow collagen solution to polymerize. The next day, cylindrical silica fibers were removed to form hollow channels (\varnothing 100 μm) and pre-flow (1 $\mu\text{L}/\text{min}$) was initiated with an incubator

gas pump (Nortis Inc. #IGP-001). Note, the MFC contains four reservoirs each with a capacity of 15 mL. During experimentation two were utilized for the constant supply and easy exchange of fresh media (30 mL total). Pumping of medium was carried out in a one-way system with fresh medium in and waste out (also collected by the remaining two reservoirs, 30 mL total). During experimentation the fresh media supply lasted up to 14 days and so did not require a reservoir to be refilled for the length of these experiments. Cells were seeded and cultured on the inner surface of the channels and within the ECM. Specifically, to model the vasculature on the MFC, a single cell suspension (2 μL of 10⁷ cells/mL) of EC (Angio-proteome #cAP-0001RFP) was injected to the bottom channel of a double-channel MFC (Nortis Inc. #DCC-001) with a Hamilton syringe. Cells were allowed to adhere for 2 h at 37°C prior to initiating flow at 1 $\mu\text{L}/\text{min}$. Culture was maintained for up to 15 days in a humidified incubator at 37 °C, 5% CO₂. Fresh EC medium was supplied every third day.

To model a vascularized tumor on the MFC we chose mRCC cancer cell spheroids [80]. Briefly, 10,000 mRCC cells were grown in suspension on low-attachment 96 well plates (Corning #7007) over the course of 48 h to allow formations of 3D cancer cell spheroids. mRCC spheroids were collected 48 h after seeding and gently mixed with chilled freshly prepared ECM. Next, 3D spheroids embedded in the collagen-based ECM were injected into the ECM chamber surrounding two silica fibers, resulting in a stochastic distribution of the spheroids with random locations. Chips were incubated for 3 h in a humidified incubator at 37 °C, 5% CO₂. Flowing ECM polymerization, silica fibers were removed from the chip to form the lumens. Pre-flow was initiated with an incubator gas pump using degassed DMEM/F12 medium (Corning #10-103). Next day DMEM/F12 medium was exchanged to EC medium (Lifeline Cell Technology #LL-0003), and EC were injected into the both lumens of a double-channel MFC. Cells were allowed to adhere for 2 h at 37 °C prior to initiating flow at 1 $\mu\text{L}/\text{min}$, this shear rate is estimated to be \sim 1.05 dyn/cm² within the parent vessel lumen providing physiological relevant conditions and simultaneously reducing medium consumption.

Flow cytometry analysis

100,000 cells were washed twice with PBS and resuspended in FACS buffer (PBS pH 7.4 with 10% (v/v) FCS). Cells were stained with a human anti-PSMA monoclonal antibody in the dark (10 $\mu\text{g}/\text{mL}$, MBL #K0142-3, mouse IgG1 clone 107-1A4). Polyclonal goat anti-mouse Ig conjugated to APC was used as a secondary antibody (2 $\mu\text{g}/\text{mL}$, BD

Pharmingen #550826). For all antibodies, cells were stained for 1 h at 4 °C in the FACS buffer. Flow cytometric profiles were acquired using a LSRFortessa II (BD Bioscience, USA) equipped with a FACSDiva analysis software. Data analysis was carried out using FCS Express 7 (version 7.08.0018).

Immunocytochemical staining

30,000 cells per well were seeded in 8 well chamber glass slide (Nunc Lab-Tek II Chamber Slide System #154534). After obtaining approximately 80% confluency cells were fixed using 4% paraformaldehyde in PBS (pH 7.4) for 10 min and blocked with 10% NGS and 0.5% Triton X-100 for 1 h at room temperature. Cells were washed with PBS and stained with primary mouse monoclonal anti-PSMA antibody (Abcam #187570) at a concentration of 1:100 overnight at 4 °C. The next day cells were washed twice with PBS and incubated with secondary anti-mouse antibodies (Alexa Fluor 488 goat anti-mouse Ig #A32723) in the concretion 1:500 for 2 h. Cell nuclei were stained for 15 min with DAPI (Thermo Fisher Scientific #D3571). Coverslips were mounted using the PermaFluor aqueous mounting medium (Thermo Scientific # TA-006-FM).

Cells cultured on the MFC were washed with PBS and fixed with fixation/permeabilization solution (BD Biosciences #554722) for 2 h at room temperature with the syringe pump (2 uL/min). Next, cells were briefly rinsed with PBS and blocked with perm/wash buffer (BD Biosciences #554723) supplemented with 2% BSA and 0.05% Tween 20 for 2 h at room temperature. Chips were incubated overnight at 4 °C with primary antibodies: mouse monoclonal anti-PSMA (Abcam #187570) and rabbit polyclonal anti-CD31 (Abcam #32457) at a concentration of 1:100 each, mixed with fresh blocking buffer and added directly to the chip. Chips were washed with 2 mL of PBS and incubated with secondary antibodies (Alexa Fluor 488 goat anti-mouse Ig #A32723, Alexa Fluor 633 goat anti-rabbit Ig #A21071) at a concentration of 1:500 for 2 h at room temperature. Unbound secondary antibodies were washed with PBS, cell nuclei were stained for 15 min with DAPI (Thermo Fisher Scientific #D3571) and chips were washed again with PBS.

Assessment of vessels functionality and patency with fluorescent beads

To test the functionality of newly formed vessels fluorescent beads of $\varnothing 10 \mu\text{m}$ (505 nm/515 nm Exc./Em.) (Thermo Fisher Scientific #F8836) and $\varnothing 15 \mu\text{m}$ (565 nm/580 nm Exc./Em.) (Thermo Fisher Scientific #F21012) were perfused through chips at

day 15. Microbeads were chosen for regional blood flow determination as these approximately match the size of immune cells. For these types of studies beads were injected in the lower channel of the chip and traveled through the vessel-like structures and the opposite channel where the fluorescence can be tracked and quantified. Beads perfused through the chip were resistant to photobleaching and retain their fluorescence.

Assessment of drug delivery

Fluorescein (Sigma #46955) was perfused through chips at days ranging from 5-10 to model drug delivery on the MFC. Fluorescein solution at a final concentration of 0.001 g/mL in regular EC medium was washed in for 2 h at 1 $\mu\text{L}/\text{min}$ through the lower channel of the chip, while the upper port remained closed. Next, the lower channel with fluorescein solution was closed and the upper port containing only EC medium was opened to wash out fluorescein. Fluorescein was washed out from ECM after 30 min and retained only in the spheroid.

Vascular targeted therapy on the microfluidic chip

Co-culture of patient derived mRCC spheroids and EC control cells was maintained until vessels were formed. 250 $\mu\text{g}/\text{mL}$ of bevacizumab [48] was added to EC medium of treated chips, while control chips were perfused with regular EC medium. Cell culture was maintained for another 3 days. Cell coverage was quantified at the beginning of the experiment (day 9), and after 3 days of treatment with bevacizumab (day 12).

Confocal microscopy, image generation, quantification, and analysis

Images were captured on a spinning disc confocal Nikon ECLIPSE Ti microscope equipped with EMCCD camera (Andor sCMOS) and laser (Lumencor SPECTRA Light Engine). Chips were imaged in a specially modified stage holder enabling chips to be imaged in their housing with sustained environmental conditions and pump connection. Confocal images were captured under white light conditions and 405 nm for DAPI channel (excitation 401 nm/emission 421 nm), 488 nm for PSMA channel (excitation 496 nm/emission 519 nm), 561 nm for RFP (excitation 555 nm/ emission 584 nm), 633 nm for CD31 channel (excitation 632 nm/emission 647 nm).

The native Nikon format was converted to 16-bit gray tiff files for quantification. In cases of suboptimal illumination conditions and to correct for stitching artefacts a fast Fourier bandpass transform was applied in Fiji (ImageJ, version 2.0.0-rc-65/1.53c).

Following image correction images were imported to MATLAB (MathWorks, version 2020b) for quantification via custom scripts. Sprouting length images were firstly thresholded and cropped followed by 2D median filtering (kernel size of 20x20 pixels) to remove artefacts. The image was then dilated using a disk-shaped dilation factor. To determine the average sprouting length the region prop's function was employed to find oval shapes the width of the image. The circumference of this oval shape accurately traced the average projection of the sprouting cells. The distance between the outer most point of this oval circumference and the upper most seeded channel point was calculated to give the average sprouting distance for a chip at a certain timepoint. The same steps were applied for all sprouting calculations.

Red fluorescent images of spheroid EC recruitment were processed in ImageJ in a similar manner as previously outlined before importing to MATLAB. A white light image consisting of the mRCC spheroid and EC was used to determine the center point of the spheroid. A custom MATLAB script was used to find the centroid coordinates of the spheroid which appeared darker and more circular than any surrounding structures and thus could be recognized by the software. Manual cropping was employed in situations in which the automated script failed to accurately identify the spheroid. The minimum distance from this center point to the closest image border along the horizontal dimension was used to crop the RFP EC fluorescent images. This resulted in images of EC centered around the spheroid. A median filter (20x20 kernel) size was applied to the thresholded binary fluorescent images followed by hole filling using the *imfill* function. The processed images were then divided up into 20 equidistant sections with the EC cellular coverage calculated for each section, elucidating the relationship between spheroid location and EC recruitment. To enable a fairer comparison between chips, 20 sections were used in all cases regardless of individual area analysis. Multiple chips as described in the images were then averaged to assess the population response. Plotting and statistical analysis were performed in either MATLAB or Prism GraphPad (version 9.0.0 (86)) with two-sided student's t-tests used to assess the null hypothesis that there was no difference between groups, with p values < 0.05 rejecting the null hypothesis.

PSMA stained on the MFC images were processed in ImageJ using a custom ImageJ script that thresholds the images leaving only the PSMA stain and applies a median filter (10x10 filter size) to remove any artefacts. Processed images were then

imported in MATLAB and analyzed via a custom script that cropped the images to the same size, divided them into 20 equidistant sections, and calculated the percentage of PSMA area in each section. The percentage area values were averaged across the three images. The 20 averaged values were passed through MATLAB *polyfit* function to generate a function describing the PSMA expression as a function of the distance from the tumor center. The *polyfit* function was also applied on the 20 percentage PSMA area values for each image separately. The location of tumor centers was measured manually by inspecting images in MATLAB. Prism GraphPad was used to plot the data obtained from the *polyfit* function in MATLAB.

Immunohistochemical staining, image quantification, and analysis

Formalin fixed paraffin embedded tumor tissues were processed by the MSKCC Molecular Cytology Core Facility. Tumor sections were stained with a primary mouse monoclonal anti-CD31 (Roche #760-4378) antibody. Next, sections were incubated with secondary Alexa Fluor 647 (Thermo Fisher Scientific # B40958) antibody. Cell nuclei were stained with DAPI (Thermo Fisher Scientific #D3571). Staining was done using automated immunohistochemical staining processor Discovery XT (Ventana Medical Systems). Images were scanned and viewed with 3DHISTECH Ltd. Case Viewer.

CD31 stained images (n = 9 control group, n = 9 treated group) were processed in ImageJ using a custom build ImageJ script that thresholds the images leaving only the CD31 stain and applies a median filter (10 pixels radius) to remove any noise in the thresholded images. Processed images were then analyzed in MATLAB using a custom script that calculates the percentage of image area occupied by CD31 stain. CD31 stained images from control and treated mice groups were averaged, statistically analyzed, and plotted in Prism GraphPad with the two-sample t-test used to assess the null hypothesis that there was no difference between the two groups, with p values < 0.05 rejecting the null hypothesis.

Assessment of angiogenesis-related proteins on the microfluidic chip

Proteomics was evaluated using an angiogenesis-focused array (R&D Systems #ARY007) to identify angiogenesis-related proteins in culture medium perfusate from the MFC. Medium was collected from the MFC maintained in culture for 15 days in different conditions: EC control perfused with regular medium, EC control co-cultured with mRCC perfused with regular medium, EC control perfused

with enriched medium, EC PSMA perfused with regular medium and EC PSMA perfused with enriched medium. Antibodies against 55 proteins were spotted in duplicate on nitrocellulose membranes. 25 mL of culture medium perfusate from each respective condition was diluted and mixed with 25 μ L of antibodies detection cocktail. Membranes were incubated for 48 h at 4 °C with antibodies. Next, membranes were washed to remove unbound material, and stained with IRDye 800CW Streptavidin (LI-COR # 926-32230) at final concentration of 1.0 μ L/mL. The Odyssey imaging system was used to detect differences in expression levels between proteins. Images were manually quantified in ImageJ using identical ROI sizes across all chips with background subtraction performed. Graphing and statistical assessment of the data was performed in Prism, see Supplemental Figure 12. Statistical significance between all conditions was determined using an Ordinary ANOVA test without matching or pairing, comparing the mean of each group via a Tukey statistical hypothesis testing. A family-wise alpha threshold of 0.05 was required for significance with a 95% confidence interval.

Animal models and vascular targeted therapy *in vivo*

Patient-derived mRCC tumors were implanted into 4-5 weeks old female NOD.Cg-Prkdc^{scid}/J mice (Jackson Laboratory) by subcutaneous injection into the upper region of the thigh of 5,000,000 cells in 100 μ L of Matrigel (Corning # 356231). To achieve this number of cells it took approximately 10-15 days of *in vitro* cell culture prior to xenografting. Tumor growth was monitored, and mice were imaged with RSOM. To track changes in the vasculature, RSOM imaging was performed 24 h before mice received the first dose of treatment, and 24 h after the last dose of treatment. Mice were administered either 6 doses of bevacizumab 20 mg/kg [49] in 50 μ L of saline solution or 50 μ L of naive saline, injected every second day for two weeks. RSOM imaging was performed under 2% v/v isoflurane inhalation anesthesia (Baxter #NDC 10019-360-60). Mice were shaved with depilatory cream before (Hair Removal Lotion, Nair) imaging to prevent light absorption and reduced image quality. All animal procedures were approved by the Institutional Animal Care and Use Committee (IACUC) and followed institutional and NIH guidelines.

Automated quantification of tumor vascular images obtained via RSOM

RSOM images were acquired using the RSOM P50 (iThera Medical, Munich, Germany) at a single

wavelength of 532 nm (hemoglobin isosbestic point). Xenografted mice were anesthetized via induction with isoflurane (3% v/v) followed by maintenance at 2% v/v. Centrifuged ultrasound gel dissolved in distilled water (30%) was applied to the imaging area using a wet cotton tipped applicator to avoid bubbles. An area of 12x12x4 mm was then imaged to assess the vascular network within the tumor for both treatment and control groups. Reconstructed images were then exported and frequency split into low (11 - 33 MHz, red) and high frequencies (33 - 99 MHz, green) to increase image fidelity. The green and red channels were then combined and exported as an 8-bit png images for automated quantification in ImageJ. A custom batch processing image analysis script was developed for the automated quantification of vascular networks as recorded by the RSOM. Firstly, the user was prompted to provide the directory location to vascular network images which were then imported and converted to 8-bit grayscale images. Once in grayscale formats the images underwent background subtraction, a tubeness filter was applied along with adaptive median filtering and thresholding. The thresholded image was quantified for area fraction before being skeletonized. The skeletonized image was then used to calculate the vascular network length and vascular network features such as number of branches, junctions, endpoints, slabs. The saved branching network data was then used to assess the tortuosity of each branch (branch length over Euclidean distance). Finally, the thresholded image prior to skeletonization was used to determine the distances between branches (nearest neighbor distance). In all cases the automated script employs built in and open access functions within the ImageJ program and exports a variety of images and excel format files including skeleton overlays for inspection and later analysis. Values for area fraction, network length, NND, branching and tortuosity were then compiled in Prism GraphPad for graphing and statistical analysis.

Supplementary Material

Supplementary figures and videos.
<https://www.thno.org/v15p0766s1.pdf>
Supplementary video 1.
<https://www.thno.org/v15p0766s2.mp4>
Supplementary video 2.
<https://www.thno.org/v15p0766s3.mp4>
Supplementary video 3.
<https://www.thno.org/v15p0766s4.mp4>
Supplementary video 4.
<https://www.thno.org/v15p0766s5.mp4>

Supplementary video 5.

<https://www.thno.org/v15p0766s6.mp4>

Acknowledgements

We thank the Abraham Hakimi Lab from MSKCC for providing us with JHRCC62A patient derived metastatic renal cell carcinoma cells. We thank Andrew Cinquina for assistance with engineering cells. We thank Ning Fan and Afsar Barlas from the MSKCC Molecular Cytology Core Facility for assistance with histology and immunohistochemistry. We also thank Thomas Neumann (Nortis) for helpful advice.

Funding

This study was funded in part by the National Cancer Institute (grant no. R01 CA212379 to JG) and by the NCI Cancer Center core grant P30 CA08748 (to Selwyn Vickers). All raw data required to validate the results in this manuscript will be uploaded and available via an open repository.

Author contributions

M.S. designed and performed all experiments, processed, and analyzed the data, and wrote the manuscript. B.M.L., J.C.D. and A.V.D. analyzed confocal microscopy and RSOM images using via scripts in both MATLAB and ImageJ based on established methods and available packages. N.B.P. and J.D. performed selected MFC experiments. A.V. and V.P. engineered cells and performed FACS. A.O. and C.L.M. provided conceptual input. J.G. supervised the study, provided input for all the experiments and the study concept, and edited the paper.

Competing Interests

The authors have declared that no competing interest exists.

References

- Hanahan D. Hallmarks of Cancer: New Dimensions. *Cancer Discov.* 2022;12(1):31-46.
- Carmeliet P, Jain RK. Angiogenesis in cancer and other diseases. *Nature.* 2000; 407(6801):249-57.
- Siemann DW, Horsman MR. Vascular targeted therapies in oncology. *Cell Tissue Res.* 2009; 335(1):241-8.
- Sharma SV, Haber DA, Settleman J. Cell line-based platforms to evaluate the therapeutic efficacy of candidate anticancer agents. *Nat Rev Cancer.* 2010; 10(4):241-53.
- Mak IW, Evaniew N, Ghert M. Lost in translation: animal models and clinical trials in cancer treatment. *Am J Transl Res.* 2014; 6(2):114-8.
- Bracken MB. Why animal studies are often poor predictors of human reactions to exposure. *J R Soc Med.* 2009; 102(3):120-2.
- Ingber DE. Human organs-on-chips for disease modelling, drug development and personalized medicine. *Nat Rev Genet.* 2022; 23(8):467-491.
- Tsai HF, Trubelja A, Shen AQ, Bao G. Tumour-on-a-chip: microfluidic models of tumour morphology, growth and microenvironment. *J R Soc Interface.* 2017; 14(131):20170137.
- Kumar V, Varghese S. Ex vivo tumor-on-a-chip platforms to study intercellular interactions within the tumor microenvironment. *Adv Healthc Mater.* 2019; 8(4):e1801198.

- Carvalho MR, Barata D, Teixeira LM, Giselbrecht S, Reis RL, Oliveira JM, et al. Colorectal tumor-on-a-chip system: A 3D tool for precision onco-nanomedicine. *Sci Adv.* 2019; 5(5):eaaw1317.
- Nashimoto Y, Okada R, Hanada S, Arima Y, Nishiyama K, Miura T, et al. Vascularized cancer on a chip: The effect of perfusion on growth and drug delivery of tumor spheroid. *Biomaterials.* 2020; 229:119547.
- Nguyen DH, Stapleton SC, Yang MT, Cha SS, Choi CK, Galie PA, et al. Biomimetic model to reconstitute angiogenic sprouting morphogenesis in vitro. *Proc Natl Acad Sci U S A.* 2013; 110(17):6712-7.
- Miller CP, Tsuchida C, Zheng Y, Himmelfarb J, Akilesh S. A 3D Human Renal Cell Carcinoma-on-a-Chip for the Study of Tumor Angiogenesis. *Neoplasia.* 2018; 20(6):610-620.
- Lyu Z, Park J, Kim KM, Jin HJ, Wu H, Rajadas J, et al. A neurovascular-unit-on-a-chip for the evaluation of the restorative potential of stem cell therapies for ischaemic stroke. *Nat Biomed Eng.* 2021; 5(8):847-863.
- Pediaditakis I, Kodella KR, Manatakis DV, Le CY, Hinojosa CD, Tien-Street W, et al. Modeling alpha-synuclein pathology in a human brain-chip to assess blood-brain barrier disruption. *Nat Commun.* 2021; 12(1):5907.
- Park TE, Mustafaoglu N, Herland A, Hasselkus R, Mannix R, FitzGerald EA, et al. Hypoxia-enhanced blood-brain barrier chip recapitulates human barrier function and shuttling of drugs and antibodies. *Nat Commun.* 2019; 10(1):2621.
- Vatine GD, Barrile R, Workman MJ, Sances S, Barriga BK, Rahnama M, et al. Human iPSC-derived blood-brain barrier chips enable disease modeling and personalized medicine applications. *Cell Stem Cell.* 2019; 24(6):995-1005.
- Sakolish C, Weber EJ, Kelly EJ, Himmelfarb J, Mouneimne R, Grimm FA, et al. Technology transfer of the microphysiological systems: a case study of the human proximal tubule tissue chip. *Sci Rep.* 2018; 8(1):14882.
- Huh D, Matthews BD, Mammoto A, Montoya-Zavala M, Hsin HY, Ingber DE. Reconstituting organ-level lung functions on a chip. *Science.* 2010; 328(5986):1662-8.
- Huh D, Leslie DC, Matthews BD, Fraser JP, Jurek S, Hamilton GA, et al. A human disease model of drug toxicity-induced pulmonary edema in a lung-on-a-chip microdevice. *Sci Transl Med.* 2012; 4(159):159ra147.
- Jalili-Firoozinezhad S, Prantil-Baun R, Jiang A, Potla R, Mammoto T, Weaver JC, Ferrante TC, et al. Modeling radiation injury-induced cell death and countermeasure drug responses in a human Gut-on-a-Chip. *Cell Death Dis.* 2018; 9(2):223.
- Jalili-Firoozinezhad S, Gazzaniga FS, Calamari EL, Camacho DM, Fadel CW, Bein A, et al. A complex human gut microbiome cultured in an anaerobic intestine-on-a-chip. *Nat Biomed Eng.* 2019; 3(7):520-531.
- Chang SY, Weber EJ, Sidorenko VS, Chapron A, Yeung CK, Gao C, et al. Human liver-kidney model elucidates the mechanisms of aristolochic acid nephrotoxicity. *JCI Insight.* 2017; 2(22):e95978.
- Sakolish C, Reese CE, Luo YS, Valdiviezo A, Schurdak ME, Gough A, et al. Analysis of reproducibility and robustness of a human microfluidic four-cell liver acinus microphysiology system (LAMPs). *Toxicology.* 2021; 448:152651.
- Weber EJ, Lidberg KA, Wang L, Bammler TK, MacDonald JW, Li MJ, et al. Human kidney on a chip assessment of polymyxin antibiotic nephrotoxicity. *JCI Insight.* 2018; 3(24):e123673.
- Ronaldson-Bouchard K, Teles D, Yeager K, Tavakol DN, Zhao Y, Chramiec A, et al. A multi-organ chip with matured tissue niches linked by vascular flow. *Nat Biomed Eng.* 2022; 6(4):351-371.
- van den Berg A, Mummery CL, Passier R, van der Meer AD. Personalised organs-on-chips: functional testing for precision medicine. *Lab Chip.* 2019; 19(2):198-205.
- Jodat YA, Kang MG, Kiaee K, Kim GJ, Martinez AFH, Rosenkranz A, et al. Human-derived organ-on-a-chip for personalized drug development. *Curr Pharm Des.* 2018; 24(45):5471-5486.
- Zhang S, Wan Z, Kamm RD. Vascularized organoids on a chip: strategies for engineering organoids with functional vasculature. *Lab Chip.* 2021; 21(3):473-488.
- Zhang B, Radisic M. Organ-on-a-chip devices advance to market. *Lab Chip.* 2017; 17(14):2395-2420.
- Padala SA, Kallam A. Clear cell renal carcinoma. *StatPearls Publishing.* 2020.
- Kalra S, Atkinson BJ, Matrana MR, Matin SF, Wood CG, Karam JA, et al. Prognosis of patients with metastatic renal cell carcinoma and pancreatic metastases. *BJU Int.* 2016; 117(5):761-5.
- Kaittanis C, Andreou C, Hieronymus H, Mao N, Foss CA, Eiber M, et al. Prostate-specific membrane antigen cleavage of vitamin B9 stimulates oncogenic signaling through metabotropic glutamate receptors. *J Exp Med.* 2018; 215(1):159-175.
- Chang SS. Overview of prostate-specific membrane antigen. *Rev Urol.* 2004;6 Suppl 10(Suppl 10):S13-8.
- Ross JS, Sheehan CE, Fisher HA, Kaufman RP Jr, Kaur P, Gray K, et al. Correlation of primary tumor prostate-specific membrane antigen expression with disease recurrence in prostate cancer. *Clin Cancer Res.* 2003; 9(17):6357-62.
- Silver DA, Pellicer I, Fair WR, Heston WD, Cordon-Cardo C. Prostate-specific membrane antigen expression in normal and malignant human tissues. *Clin Cancer Res.* 1997; 3(1):81-5.
- Chang SS, O'Keefe DS, Bacich DJ, Reuter VE, Heston WD, Gaudin PB. Prostate-specific membrane antigen is produced in tumor-associated neovasculature. *Clin Cancer Res.* 1999; 5(10):2674-81.

38. Baccala A, Sercia L, Li J, Heston W, Zhou M. Expression of prostate-specific membrane antigen in tumor-associated neovasculature of renal neoplasms. *Urology*. 2007; 70(2):385-90.
39. Nomura N, Pastorino S, Jiang P, Lambert G, Crawford JR, Gymnopoulos M, et al. Prostate specific membrane antigen (PSMA) expression in primary gliomas and breast cancer brain metastases. *Cancer Cell Int*. 2014; 14(1):26.
40. Wernicke AG, Varma S, Greenwood EA, Christos PJ, Chao KS, Liu H, et al. Prostate-specific membrane antigen expression in tumor-associated vasculature of breast cancers. *APMIS*. 2014; 122(6):482-9.
41. Chang SS, Reuter VE, Heston WD, Bander NH, Grauer LS, Gaudin PB. Five different anti-prostate-specific membrane antigen (PSMA) antibodies confirm PSMA expression in tumor-associated neovasculature. *Cancer Res*. 1999; 59(13):3192-8.
42. Watanabe R, Maekawa M, Kiyoi T, Kurata M, Miura N, Kikugawa T, et al. PSMA-positive membranes secreted from prostate cancer cells have potency to transform vascular endothelial cells into an angiogenic state. *Prostate*. 2021; 81(16):1390-1401.
43. Machado CML, Skubal M, Haedicke K, Silva FP, Stater EP, Silva TLAO, et al. Membrane-derived particles shed by PSMA-positive cells function as pro-angiogenic stimuli in tumors. *J Control Release*. 2023; 364:312-325.
44. Kazazi-Hyseni F, Beijnen JH, Schellens JH. Bevacizumab. *Oncologist*. 2010; 15(8):819-25.
45. Haedicke K, Agemy L, Omar M, Bereznoi A, Roberts S, Longo-Machado C, et al. High-resolution optoacoustic imaging of tissue responses to vascular-targeted therapies. *Nat Biomed Eng*. 2020; 4(3):286-297.
46. Bock F, Onderka J, Dietrich T, Bachmann B, Kruse FE, Paschke M, et al. Bevacizumab as a potent inhibitor of inflammatory corneal angiogenesis and lymphangiogenesis. *Invest Ophthalmol Vis Sci*. 2007; 48(6):2545-52.
47. Al-Ahmadie HA, Olgac S, Gregor PD, Tickoo SK, Fine SW, Kondagunta GV, et al. Expression of prostate-specific membrane antigen in renal cortical tumors. *Mod Pathol*. 2008; 21(6):727-32.
48. Hein M, Graver S. Tumor cell response to bevacizumab single agent therapy in vitro. *Cancer Cell Int*. 2013; 13(1):94.
49. Cao S, Durrani FA, Toth K, Rustum YM, Seshadri M. Bevacizumab enhances the therapeutic efficacy of Irinotecan against human head and neck squamous cell carcinoma xenografts. *Oral Oncol*. 2011; 47(6):459-66.
50. Lopes-Coelho F, Martins F, Pereira SA, Serpa J. Anti-Angiogenic Therapy: Current Challenges and Future Perspectives. *Int J Mol Sci*. 2021; 22(7):3765.
51. Carmeliet P. VEGF as a key mediator of angiogenesis in cancer. *Oncology*. 2005; 69 Suppl 3:4-10.
52. Murakami M, Simons M. Fibroblast growth factor regulation of neovascularization. *Curr Opin Hematol*. 2008; 15(3):215-20.
53. Cross MJ, Claesson-Welsh L. FGF and VEGF function in angiogenesis: signalling pathways, biological responses and therapeutic inhibition. *Trends Pharmacol Sci*. 2001; 22(4):201-7.
54. Osaki T, Kakegawa T, Kageyama T, Enomoto J, Nittami T, Fukuda J. Acceleration of vascular sprouting from fabricated perfusable vascular-like structures. *PLoS One*. 2015; 10(4):e0123735.
55. Thoma CR, Zimmermann M, Agarkova I, Kelm JM, Krek W. 3D cell culture systems modeling tumor growth determinants in cancer target discovery. *Adv Drug Deliv Rev*. 2014; 69-70:29-41.
56. Kimlin LC, Casagrande G, Virador VM. In vitro three-dimensional (3D) models in cancer research: an update. *Mol Carcinog*. 2013; 52(3):167-82.
57. Heesch A, Ortmanns L, Maurer J, Stickeler E, Sahnoun SEM, Mottaghy FM, et al. The Potential of PSMA as a Vascular Target in TNBC. *Cells*. 2023; 12(4):551.
58. Winkler J, Abisoye-Ogunniyan A, Metcalf KJ, Werb Z. Concepts of extracellular matrix remodelling in tumour progression and metastasis. *Nat Commun*. 2020; 11(1):5120.
59. Conway RE, Petrovic N, Li Z, Heston W, Wu D, Shapiro LH. Prostate-specific membrane antigen regulates angiogenesis by modulating integrin signal transduction. *Mol Cell Biol*. 2006; 26(14):5310-24.
60. Wu MH, Huang CY, Lin JA, Wang SW, Peng CY, Cheng HC, et al. Endothelin-1 promotes vascular endothelial growth factor-dependent angiogenesis in human chondrosarcoma cells. *Oncogene*. 2014; 33(13):1725-35.
61. van Crujisen H, Giaccone G, Hoekman K. Epidermal growth factor receptor and angiogenesis: Opportunities for combined anticancer strategies. *Int J Cancer*. 2005; 117(6):883-8.
62. Lien MY, Chang AC, Tsai HC, Tsai MH, Hua CH, Cheng SP, et al. Monocyte chemoattractant protein 1 promotes VEGF-A expression in OSCC by activating ILK and MEK1/2 signaling and downregulating miR-29c. *Front Oncol*. 2020; 10:592415.
63. O'Reilly MS, Boehm T, Shing Y, Fukai N, Vasios G, Lane WS, et al. Endostatin: an endogenous inhibitor of angiogenesis and tumor growth. *Cell*. 1997; 88(2):277-85.
64. Tigner A, Ibrahim SA, Murray IV. Histology, White Blood Cell. [Updated 2022 Nov 14]. In: StatPearls [Internet]. Treasure Island (FL): StatPearls Publishing; 2024 Jan-.
65. Binnewies M, Roberts EW, Kersten K, Chan V, Fearon DF, Merad M, et al. Understanding the tumor immune microenvironment (TIME) for effective therapy. *Nat Med*. 2018; 24(5):541-550.
66. Jun JV, Chenoweth DM, Petersson EJ. Rational design of small molecule fluorescent probes for biological applications. *Org Biomol Chem*. 2020; 18(30):5747-5763.
67. Du Le VN, Patterson MS, Farrell TJ, Hayward JE, Fang Q. Experimental recovery of intrinsic fluorescence and fluorophore concentration in the presence of hemoglobin: spectral effect of scattering and absorption on fluorescence. *J Biomed Opt*. 2015; 20(12):127003.
68. Cavallo C, De Laurentis C, Vetrano IG, Falco J, Broggi M, Schiariti M, et al. The utilization of fluorescein in brain tumor surgery: a systematic review. *J Neurosurg Sci*. 2018; 62(6):690-703.
69. Zeh R, Sheikh S, Xia L, Pierce J, Newton A, Predina J, et al. The second window ICG technique demonstrates a broad plateau period for near infrared fluorescence tumor contrast in glioblastoma. *PLoS One*. 2017; 12(7):e0182034.
70. Escudier B, Pluzanska A, Koralewski P, Ravaud A, Bracarda S, Szczylk C, et al. Bevacizumab plus interferon alfa-2a for treatment of metastatic renal cell carcinoma: a randomised, double-blind phase III trial. *Lancet*. 2007; 370(9605):2103-11.
71. Bose S, Clevers H, Shen X. Promises and challenges of organoid-guided precision medicine. *Med*. 2021; 2(9):1011-1026.
72. Mathur L, Ballinger M, Utharala R, Merten CA. Microfluidics as an enabling technology for personalized cancer therapy. *Small*. 2020; 16(9):e1904321.
73. Han JJ. FDA Modernization Act 2.0 allows for alternatives to animal testing. *Artif Organs*. 2023; 47(3):449-450.
74. Tourovskaia A, Fauver M, Kramer G, Simonson S, Neumann T. Tissue-engineered microenvironment systems for modeling human vasculature. *Exp Biol Med (Maywood)*. 2014; 239(9):1264-71.
75. Radaelli E, Santagostino SF, Sellers RS, Brayton CF. Immune Relevant and Immune Deficient Mice: Options and Opportunities in Translational Research. *ILAR J*. 2018; 59(3):211-246.
76. Dong Y, Manley BJ, Becerra MF, Redzematovic A, Casucelli J, Tennenbaum DM, et al. Tumor xenografts of human clear cell renal cell carcinoma but not corresponding cell lines recapitulate clinical response to sunitinib: feasibility of using biopsy samples. *Eur Urol Focus*. 2017; 3(6):590-598.
77. Van Ness KP, Chang SY, Weber EJ, Zumpano D, Eaton DL, Kelly EJ. Microphysiological Systems to Assess Nonclinical Toxicity. *Curr Protoc Toxicol*. 2017; 73:14.18.1-14.18.28.
78. Aisenbrey EA, Murphy WL. Synthetic alternatives to Matrigel. *Nat Rev Mater*. 2020; 5(7):539-551.
79. Cross VL, Zheng Y, Won Choi N, Verbridge SS, Sutermeister BA, Bonassar LJ, et al. Dense type I collagen matrices that support cellular remodeling and microfabrication for studies of tumor angiogenesis and vasculogenesis in vitro. *Biomaterials*. 2010; 31(33):8596-607.
80. Pereira PMR, Berisha N, Bhupathiraju NVSDK, Fernandes R, Tomé JPC, Drain CM. Cancer cell spheroids are a better screen for the photodynamic efficiency of glycosylated photosensitizers. *PLoS One*. 2017; 12(5):e0177737.